Cavity-Enhanced Measurements of Defect Spins in Silicon Carbide

Greg Calusine,[1] Alberto Politi,[1,2] and David D. Awschalom[1,3,*]

[1]*Department of Physics, University of California, Santa Barbara, California 93106, USA*
[2]*School of Physics and Astronomy, University of Southampton, Southampton SO17 1BJ, United Kingdom*
[3]*Institute for Molecular Engineering, University of Chicago, Chicago, Illinois 60637, USA*

(Received 7 October 2015; revised manuscript received 13 March 2016; published 29 July 2016)

The identification of new solid-state defect-qubit candidates in widely used semiconductors has the potential to enable the use of nanofabricated devices for enhanced qubit measurement and control operations. In particular, the recent discovery of optically active spin states in silicon carbide thin films offers a scalable route for incorporating defect qubits into on-chip photonic devices. Here, we demonstrate the use of 3C silicon carbide photonic crystal cavities for enhanced excitation of color-center defect spin ensembles in order to increase measured photoluminescence signal count rates, optically detected magnetic-resonance signal intensities, and optical spin initialization rates. We observe an up to a factor of 30 increase in the photoluminescence and optically detected magnetic-resonance signals from Ky5 color centers excited by cavity-resonant excitation and increase the rate of ground-state spin initialization by approximately a factor of 2. Furthermore, we show that the 705-fold reduction in excitation mode volume and enhanced excitation and collection efficiencies provided by the structures can be used to overcome inhomogenous broadening in order to facilitate the study of defect-qubit subensemble properties. These results highlight some of the benefits that nanofabricated devices offer for engineering the local photonic environment of color-center defect qubits to enable applications in quantum information and sensing.

DOI: 10.1103/PhysRevApplied.6.014019

I. INTRODUCTION

Electronic spins associated with color-center defects in silicon carbide (SiC) show promise as a potential component for solid-state quantum technologies due to their combination of long coherence times [1], room-temperature operation [2], and a host material for which mature growth [3] and fabrication protocols exist [4]. The ability to engineer the local photonic environment of optically active solid-state qubits through the use of microfabrication techniques is crucial for their scalable application to the field of quantum information [5]. In contrast to the most widely studied forms of SiC (4*H* and 6*H*), the availability of cubic 3*C*-SiC as a single-crystal heteroepitaxial layer on silicon opens up the possibility of combining the favorable properties of SiC defect qubits with the fabrication capabilities available in III–V and silicon-on-insulator semiconductor systems. This may enable on-chip, scalable architectures for generating [6], routing [7], manipulating [8], and detecting [9] single-photon emission from defect qubits in SiC. These capabilities can be combined with small-mode-volume optical cavities [10–14] to utilize strong Purcell enhancements [7,15] for efficient single-photon generation or to use cavity QED protocols to realize a spin-photon interface [16] as a node in an optically connected "quantum network" [17,18].

To date, only modest quality factors ("Q") of up to 1550 have been demonstrated for small-mode-volume ("V_m") cavities [$V_m \sim (\lambda/n)^3$] operating at wavelengths relevant for coupling to known defect-qubit optical transitions in 3*C*-SiC [19]. Nevertheless, low- and modest-Q microcavities can be used to improve defect-qubit optical readout and control schemes. More specifically, microcavities can be used to compensate for limited laser power budgets and on-chip power-coupling limitations [20] in order to facilitate optical coherent control schemes [21], generate on-chip frequency conversion [22], and improve rates of absorption and fluorescence for color-center-based sensing applications [23–25]. In this work, we utilize cavity-resonant excitation to increase the photoluminescence (PL) count rate, optically detected magnetic-resonance (ODMR) signal intensity, and rate of spin-state initialization for Ky5 defect spin ensembles incorporated into 3*C*-SiC photonic crystal cavities. Furthermore, we use these signal improvements and techniques to study inhomogeneity in the Ky5 defect spin and optical properties and extract estimates of the defects' sublevel transition rates.

The Ky5 point defect is a color center in 3*C*-SiC that has been previously demonstrated to exhibit spin and optical properties that are similar to the negatively charged nitrogen vacancy (NV) center in diamond [26]. It produces an optical emission band consisting of a zero phonon line (ZPL) around 1118 nm and a redshifted phonon sideband extending out to approximately 1300 nm and, like the NV center, its $S = 1$ spin ground state can be initialized and

*awsch@uchicago.edu

read out optically. Spin coherence times (T_2) in excess of 20 μs have been demonstrated for the ground-state spin sublevels of Ky5 ensembles. These states can be manipulated with resonant microwave pulses on fast time scales (tens of nanoseconds) even up to room temperature, making Ky5 centers a viable candidate for a defect-based spin qubit. The Ky5 center can be controllably generated within the 3C-SiC crystal lattice through a combination of radiation damage and subsequent annealing and has been tentatively identified as a neutral divacancy [27]. Because of the availability of 3C-SiC as a heteroepitaxial film on silicon, photonic structures with three-dimensional optical confinement can be fabricated by removing the underlying substrate through conventional silicon wet and dry etch processes.

II. CAVITY-ENHANCED EXCITATION AND MEASUREMENT

The use of on-chip photonic cavities to enhance defect-qubit excitation is analogous to the use of macroscopic enhancement cavities to generate large intracavity optical fields for applications such as high-sensitivity absorption spectroscopy in atomic gases [28] or efficient nonlinear optical frequency conversion. In general, for a fixed-incident excitation power, the local electric-field intensity inside a microcavity scales as $|E|^2 \propto \eta Q/V_m$, where η is the input power-coupling efficiency. More specifically, temporal coupled-mode theory can be used to calculate the response of a photonic crystal cavity subject to far-field excitation by an externally incident Gaussian beam, yielding the expression

$$\frac{|E_c|^2}{|E_0|^2} = \frac{Q\eta\lambda n_o w_o^2}{4n_c^2 V_m}, \tag{1}$$

where $|E_c|^2$ is the cavity electric-field intensity maximum, $|E_0|^2$ is the incident-beam electric-field intensity maximum, λ is the wavelength of the cavity mode, n_o is the refractive index of the medium surrounding the cavity, w_o is the incident-beam waist, and n_c is the cavity index of refraction (~2.64 for 3C-SiC) [29]. Alternatively, finite-difference time-domain simulations [30,31] can be used to directly calculate the steady-state response of the cavity to continuous wave excitation. Figure 1(a) shows the excitation geometry we use to simulate the local field enhancement generated in a 300-nm-thick L3 cavity for an incident Gaussian electric-field intensity with unity amplitude and beam waist equal to our experimentally measured value of ~1 μm. The resulting simulated electric-field intensity enhancement of 193.48 agrees within 1% of the value of calculated from Eq. (1) using the input parameters extracted from simulations for the L3 cavity design. See Ref. [29] for a comparison of the local field enhancements and cavity parameters for different structure designs and a more detailed discussion of the simulations.

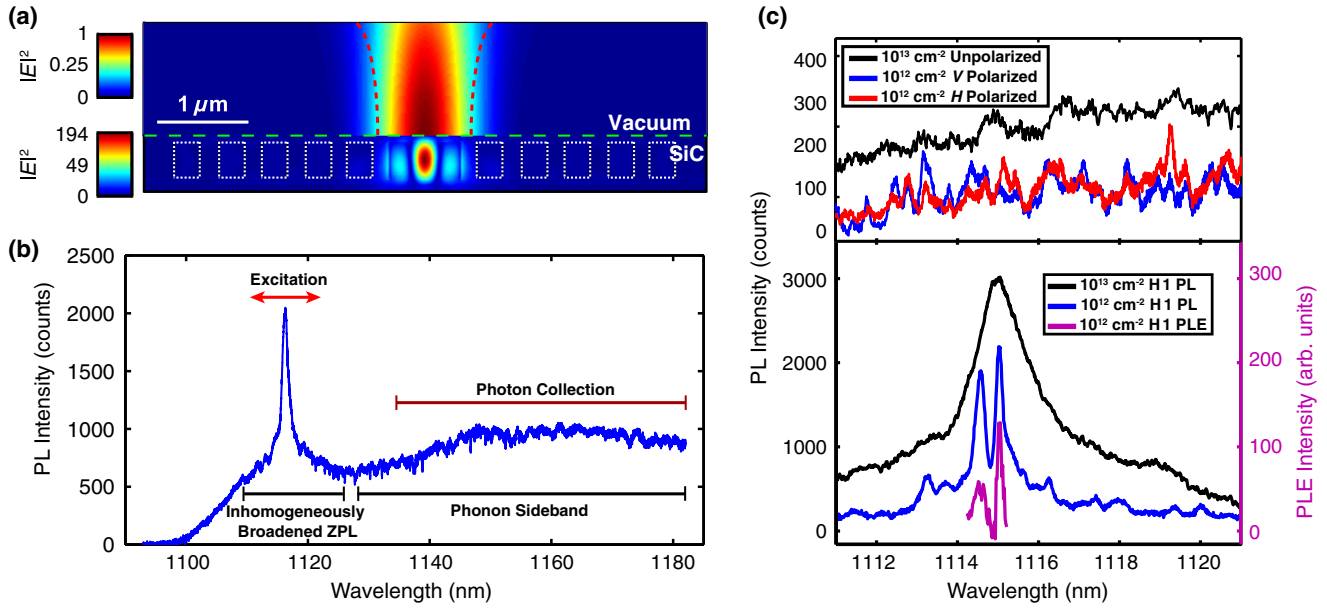

FIG. 1. (a) Simulation of the L3 cavity electric-field intensity enhancement relative to an incident Gaussian beam (1-μm beam waist indicated by the dashed red lines) with unity electric-field amplitude maximum. Note the change in scale above and below the dashed green line. The dashed white lines delineate the cross sections of the photonic-crystal-cavity holes. (b) Diagram depicting the CEPLE scheme overlaid on top of the off-resonantly-excited PL spectrum of an L3 cavity with incorporated Ky5 centers at 20 K. (c) (top panel) Fine structure within the Ky5 ZPL for different implantation doses. (bottom panel) H1 cavity resonances in the Ky5 fluorescence spectrum for films with different implantation doses (black and blue lines) and corresponding PLE measurements of the observed fine structure (magenta line). All curves are scaled for ease of comparison.

Cavity-resonant excitation also has the benefit of exciting a significantly smaller sample volume than a standard objective lens configuration. The excitation volume of a thin film is greatly reduced as compared to that of bulk material because the excitation volume dimension along the optical axis is set by the thickness of the thin film rather than the diffraction limit ($\sim$10 μm for a 0.7 NA objective at $\lambda = 1.1$ μm [32]). For our optical configuration, the cavity provides a further 12.4-fold reduction in the sample excitation volume as compared to the thin film, resulting in an overall 705-fold reduction as compared to bulk material [29]. This reduction in the excitation of localized states in the proximity of isolated single emitters within the surrounding material can improve the performance of single-photon sources by reducing background fluorescence [33] or charge-induced spectral diffusion [34].

To observe cavity-enhanced excitation, we measure photonic crystal cavities that were designed to exhibit fundamental modes tuned to the inhomogeneously broadened ZPL of the Ky5 centers incorporated into the cavity [around 1118 nm, see Fig. 1(b)]. The cavities consist of L3 and H1 structures fabricated in 300-nm-thick 3*C*-SiC films that are implanted with carbon ions at an energy of 110 KeV and annealed at 750 °C for 30 min in order to generate ensembles of Ky5 defects. Details of the sample design, fabrication, and characterization are presented in Ref. [19]. We primarily focus on L3 designs to observe cavity-enhanced optical excitation due to their greater degree of coupling to far-field Gaussian modes as compared to the H1 cavities, which are better suited for improved narrow-band collection of off-resonantly-excited defect PL [35]. The measured L3 structures exhibit $Q \sim 900$ with simulated mode volumes of 0.68 $(\lambda/n)^3$ and far-field coupling efficiencies to external, free-space Gaussian modes of 9.6% [29].

All measurements are performed in a homebuilt scanning confocal microscope with an integrated helium flow cryostat at 20 K. A 1064-nm diode laser is used for off-resonant excitation and a tunable (1090–1180 nm), narrow linewidth ($<$ 300 kHz) Littman-Metcalf diode laser is used for resonant photoluminescence excitation and cross-polarized resonant scattering spectroscopy [36]. Samples are mounted with the cavity axis at 45° with respect to the incident laser polarization to allow for the use of the latter technique for control measurements. Collected PL and reflected laser light passes back through the objective and is detected using an InGaAs CCD array, a low-noise femtowatt photoreceiver, or a superconducting nanowire single-photon detector. See Ref. [29] for a detailed description of the experimental apparatus and control measurements.

Figure 1(b) shows the off-resonantly-excited PL spectrum of a 3*C*-SiC thin film that is implanted at a dose of 10^{13} ions per square centimeter and patterned into an L3 cavity. The cavity mode is visible as a narrow peak in the spectrum at 1117.1 nm on top of the inhomogenously broadened ZPL (FWHM $\approx$ 28.2 nm). This degree of inhomogenous broadening is also present in Ky5 defects located near the Si-SiC growth interface in unpatterned thin films. For films implanted at a dose of 10^{13} ions per square centimeter, the cavity mode results in a smooth Lorentzian line shape because the Ky5 ZPL spectral density is fairly flat over the linewidth of the cavity, albeit with some luminescence fine structure and ambient moisture absorption lines [see Fig. 1(c), top panel, black line]. For films implanted at a lower dose of 10^{12} ions per square centimeter, luminescence fine structure is readily apparent as a series of polarization-dependent peaks clustering around the ZPL center wavelength [Fig. 1(c), top panel, blue and red lines]. Similar spectra have been observed previously for optical emitters subject to inhomogenous broadening [37,38] and have been attributed to statistical fluctuations in emitter spectral density. This model of statistical fine structure estimates that $\sim$200 Ky5 centers emit within the homogenous linewidth at the peak of the inhomogeneously broadened ZPL in these thin films.

This fine structure has a dramatic effect on the cavity resonance line shape when the films are processed into a photonic crystal resonator, as shown in the bottom panel of Fig. 1(c) (blue line). We observe up to a 20$\times$ enhancement in the luminescence intensity on-resonance for Ky5 ensembles incorporated into H1 photonic crystal cavities, and due to the small cavity-mode volume and polarized far-field emission pattern, this allows us to more easily isolate luminescence lines that result from this fine structure. As a result, we are able to isolate luminescence peaks exhibiting fluorescence linewidths as narrow as 25 GHz within the broader ensemble ZPL. Furthermore, we use the cavity's small mode volume and intense local excitation field to perform cavity-enhanced photoluminescence spectroscopy (CEPLE) on these narrow spectral features. CEPLE is performed by tuning the excitation wavelength to the cavity resonance peak where the light is absorbed by exciting the ZPL transitions and collecting the redshifted sideband PL, as depicted in Fig. 1(b). Figure 1(c) (magenta line) shows the CEPLE spectrum of the narrow luminescence lines shown in Fig. 1(c) (blue line). These results confirm the $\sim$25 GHz fine-structure linewidth and demonstrate significantly higher PL count rates ($\sim$1400 counts/s vs $\sim$200 counts/s) using significantly lower excitation powers (1.5 μW vs 3.2 mW) as compared with narrow-band collection of the off-resonantly-excited PL using a scanning monochromator. Similar to previous studies of fluorescence from ensembles of color centers in microcavities [39], we observe no Purcell enhancement or reduction of the fluorescence emission rate due to the effects of ensemble averaging. For further details on Ky5 ensemble fine structure, see Ref. [29].

In order to determine the total PL signal count-rate increase achieved by cavity-enhanced excitation as compared with the unpatterned, released thin film, we perform a

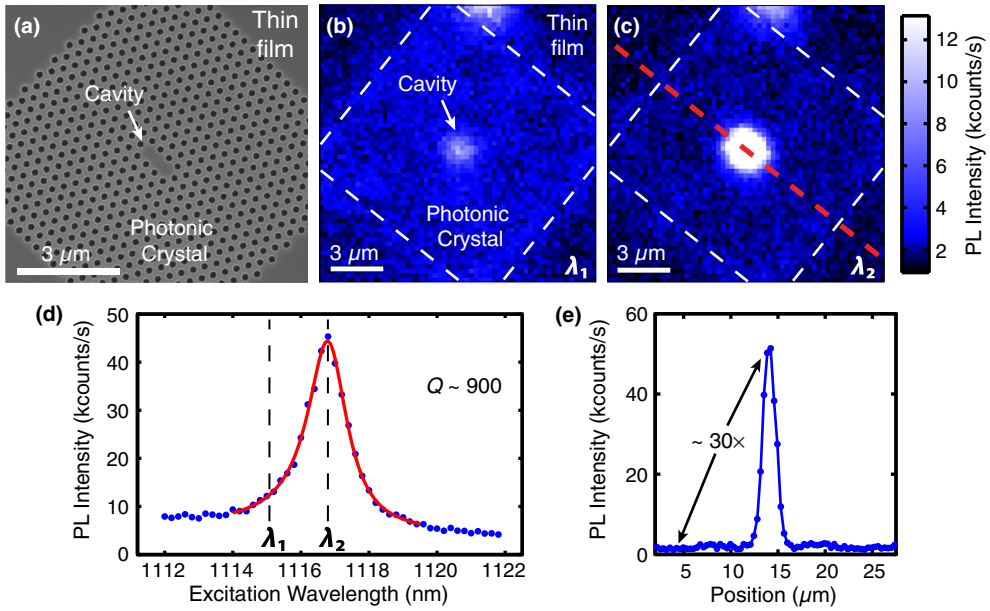

FIG. 2. (a) SEM image of the 3*C*-SiC L3 cavity structure. (b) and (c) 15 μm $\times$ 15 μm spatial scans of the sideband PL intensity signal for the excitation wavelengths depicted in (d) [(b) $\lambda_1 = 1115.1$ nm, (c) $\lambda_2 = 1117.1$ nm]. The white dashed lines indicate the extent of the photonic crystal. The count rate measured on the cavity in (c) is ~48 kcounts/s. (d) Sideband PL count rate vs excitation wavelength measured at the position of the cavity. (e) Linecut along the dashed red line in (c).

series of spatial scans over the photonic-crystal-cavity area in an L3 cavity implanted at a dose of 10^{13} ions per square centimeter and compare the overall cavity PL count rate to that of the surrounding thin film. Figure 2(a) shows a scanning electron microscope (SEM) image of the L3 cavity and Figs. 2(b) and 2(c) show a pair of scanning confocal PL images of a 12 μm $\times$ 12 μm L3 photonic crystal cavity with excitation wavelengths as designated in Fig. 2(d). The photonic crystal extent is delineated by the white dashed lines and the bright spot in its center is fluorescence originating from the cavity. The excitation wavelength-dependent PL count rate originating from the cavity location shown in Fig. 2(d) matches the cavity-mode spectrum and the peak exhibits an approximately factor of 5 increase over off-resonant excitation. Figure 2(e) shows a linecut of the PL map corresponding to the red dashed line in Fig. 2(c).

At the excitation wavelength corresponding to the cavity resonance, the PL count rate is approximately $\Gamma \approx 30$ times higher than the PL count rate from the unpatterned thin film, where we define Γ as the ratio of the resonantly-excited-cavity PL count rate to the thin film PL count rate at the same excitation wavelength and power. For H1 designs, we observe a lower maximum $\Gamma \approx 13$ due to a smaller degree of input coupling for an incident Gaussian beam. For each of these measured values of Γ, the PL count rate remains linearly proportional to input excitation power (no fluorescence saturation is observed at this Ky5 center density). Additionally, we verify that scattered laser light adds a negligible contribution to the measured signal (see Ref. [29]). While we excite cavity modes tuned to the Ky5 defect ZPL wavelength range, this same approach can be applied to applications that require efficient off-resonant excitation [40] and would be particularly beneficial for excitation wavelengths that overlap weakly with the defects' absorption spectrum.

The observed signal improvements provide a means to greatly increase the ODMR signal amplitude in order to probe the Ky5 center's spin-dependent electronic structure or for subdiffraction limit, on-chip sensing applications. In order to perform spin-dependent measurements on defects within the cavity structure, we perform an additional fabrication step that adds a 10 nm/300 nm Ti/Au metallization layer to the sample surface for applying intense local microwave fields to the sample. Figure 3(a) shows an optical image of an array of released 3*C*-SiC films patterned with photonic crystal cavities next to a 50-μm-wide microstrip positioned 50 μm away from the structures. Because of the robustness of the approximately 40 μm $\times$ 40 μm freestanding films, the metallization can be applied prior to or after the membrane release step without the need for critical point drying. We use on-chip microstrips in order to apply sufficiently intense microwave fields to achieve coherent spin manipulation (Rabi oscillations) on time scales faster than the Ky5 defects' T_2^* of ~50 ns [26].

Figure 3(b) compares the Ky5 ODMR signal (Δ_{PL}) with the excitation beam incident on the released 3*C*-SiC thin film (black line and dots) and the photonic crystal cavity (red line and dots) for the same optical power at zero magnetic field. For both ODMR curves, the $m_s = 0$ and $m_s = \pm 1$ spin sublevel transitions are saturated with microwave excitation and no change in ODMR contrast is observed. The overall ODMR signal increase matches the PL count-rate increase observed for this cavity ($\Gamma \approx 20$), further confirming that the PL count rate increases under resonant excitation originate from defect PL rather than scattered excitation. This measurement signal enhancement

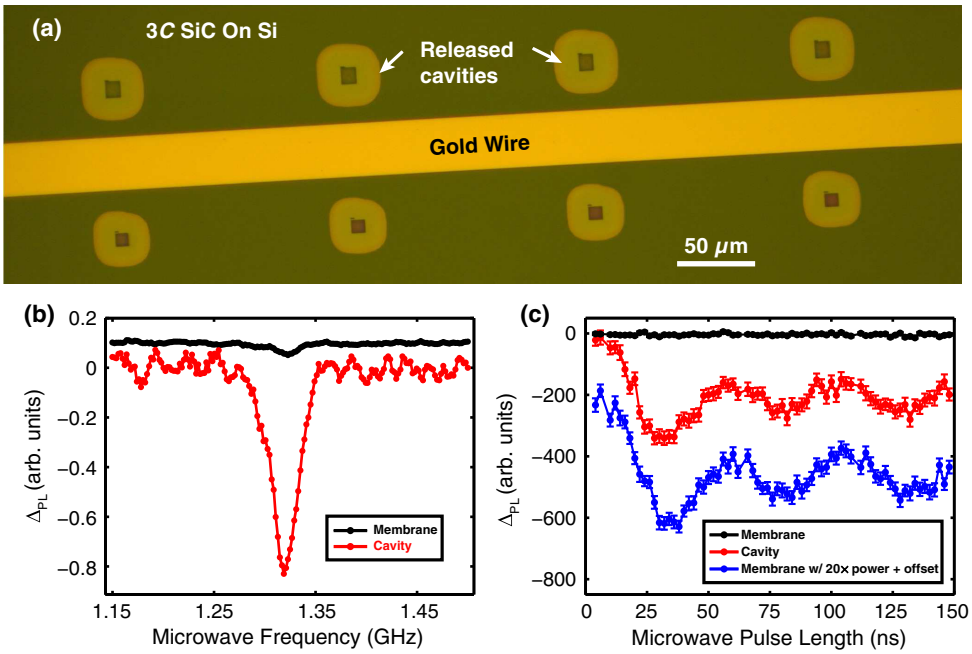

FIG. 3. (a) Optical image of a photonic-crystal-cavity array with a 50-μm-wide 10 nm/300 nm Ti/Au microstrip positioned 50 μm away from the cavities. (b) ODMR signal at 1.319 GHz measured on the photonic crystal cavity (black line and dots) and on the 3*C*-SiC thin film (red line and dots) for excitation at the same power at the cavity resonance wavelength. (c) Pulsed ODMR signal from a Ky5 ensemble subject to cavity-enhanced excitation (red line and dots) as compared to an ensemble within the thin film (black line and dots). The blue line and dots show the same measurement for defects within the thin film for a higher optical-excitation power (offset for clarity).

and reduction in the number of measured emitters afforded by the cavity can be used to facilitate studies of the optical and spin inhomogeneity that we observe for defects in 3*C*-SiC thin films [19,29,41,42]. For example, in high-emitter-density samples (10^{13} ions per square centimeter implantation dose) like those measured in Fig. 3, we observe variations in the defect ground-state zero-field splitting ($D \approx 1.32$ GHz) of up to 10 MHz and variations in the ensemble ODMR linewidth by almost a factor of 2 as the excitation wavelength is varied within the inhomogeneously broadened ensemble ZPL.

III. ENHANCED SPIN INITIALIZATION RATES

Similar signal improvements are observed for pulsed ODMR signals, as depicted in Fig. 3(c). By synchronizing pulsed optical excitation to polarize and read out the spin ensemble with pulsed microwaves for spin manipulation, we observe Rabi oscillations between the $m_s = 0$ and $m_s = \pm 1$ spin sublevels of the defects' ground states for emitters excited via the cavity mode or in the unpatterned thin film. For pulsed ODMR measurements, the signal is greatly increased under resonant excitation due to a combination of both higher PL count rates and the fact that the excitation enhancement provided by the resonant cavity mode can also be used to increase the rate of optically induced spin polarization in the Ky5 defects' ground state. To observe the latter process, we measure the defects' time-dependent PL intensity in response to variable-length laser pulses with interleaved microwave π pulses driving the $m_s = 0$ to $m_s = \pm 1$ ground-state spin sublevel transitions as shown in Fig. 4(a). A series of optical pulses with a variable length from 250 to 1500 ns is applied to excite the Ky5 defects from the ground state to the excited state where they experience either spin-conserving radiative recombination or spin-dependent relaxation to the ground-state spin sublevels predominantly via the intersystem crossing (ISC) transitions [43]. As a result of this relaxation pathway, optical excitation achieves ground-state spin polarization at a rate that depends on the optical-excitation pulse length and field intensity. Relaxation through the ISC transitions also provides a means for reading out the spin state: for a period of time immediately after the turn on of the optical pulse, the Ky5 defects will fluorescence more or less brightly depending on the ground-state spin polarization immediately prior to the optical pulse. Accordingly, we collect the PL for a fixed time period of 100 ns immediately after the turn on of the optical pulse to obtain a measure of the spin polarization generated by the previous pulse. Prior to half of the optical pulses, we apply a microwave π pulse to invert the ground-state spin polarization, which is then repumped to the steady-state polarization by the subsequent optical excitation. We measure this difference in PL ($\mathrm{PL}_{|0\rangle} - \mathrm{PL}_{|\pm 1\rangle}$) between optical pulses that immediately follow a π pulse and those that do not to obtain a measure of the ground-state spin polarization. The optical excitation is turned off for at least 500 ns prior to microwave manipulation and readout to allow for population within the ISC levels to fully relax to the ground state.

The same model used to explain the PL dynamics of other optically polarized color centers exhibiting intersystem crossing levels (OPCCs) can be applied to model Ky5 center optical dynamics [43,44]. Figure 4(b) shows the results of numerical simulations of the time-dependent difference in PL between a generic OPCC that has been initially prepared in the $m_s = 0$ state and the $m_s = \pm 1$

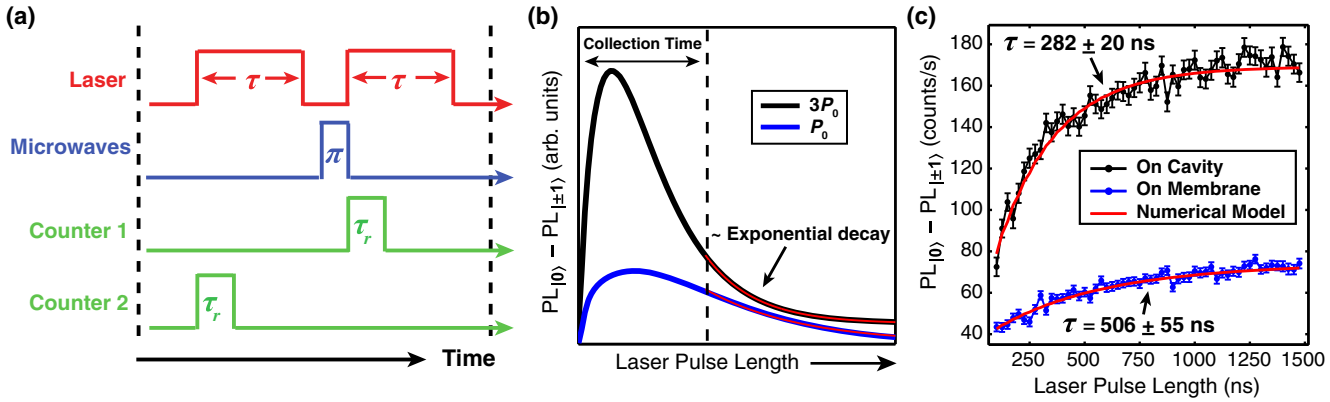

FIG. 4. (a) Pulse sequences for measuring spin-dependent PL dynamics of Ky5 centers using a variable-length laser excitation pulse (not to scale). (b) Simulated time-dependent difference in PL for a generic OPCC initialized into the $m_s = 0$ vs $m_s = \pm 1$ ground state for two excitation rates differing by a factor of 3. The red lines depict exponential fits to the time scales that correspond to an approximately exponential saturation of the ground-state spin polarization. The black curve is offset for clarity. (c) Measured PL difference signal for an ensemble of Ky5 defects within an L3 photonic crystal cavity excited on resonance (black line and dots) as compared with an ensemble excited within the unpatterned thin film (blue line and dots) at the same power and wavelength. The red lines represent simulated behavior as predicted by the model discussed in the main text. The time constants result from exponential fits to the data.

states for two excitation rates differing by a factor of 3. The figure also depicts the measurement scheme described above and the approximately exponential decay of the PL difference curves for laser-pulse lengths longer than the collection time (red lines). This limiting behavior corresponds to an approximately exponentially saturating ground-state spin polarization and PL difference signal. We observe corresponding behavior when comparing the laser-pulse length-dependent PL difference signal for Ky5 defects excited within the thin film with those excited using the photonic-crystal-cavity mode, as shown in Fig. 4(c). Figure 4(c) also shows the results of numerical simulations of this difference signal for varying laser-pulse lengths. The observed saturation behavior matches the predicted dynamics for intersystem crossing rates that differ from previously studied OPCCs such as the NV center in diamond, as determined from a nonlinear least-squares fit to a numerical model that includes the expected excitation enhancement ($|E_c|^2/|E_0|^2 \sim 96$) for this structure geometry [29]. The enhanced excitation rate for defects within the cavity structure generates a faster rate of ground-state spin initialization corresponding to a shorter time constant τ. The time constant associated with this approximately exponential saturation of the PL difference signal decreases from $\tau = 500 \pm 55$ ns to $\tau = 280 \pm 20$ ns. This approximately factor of 2 difference in the time constant for optical pumping is relatively small as compared to the overall PL count-rate increase ($\sim 20\times$) because for high excitation rates, the spin initialization rate becomes limited by the transition rate to the intersystem crossing levels rather than the rate of optical cycling. As a control measurement to verify the spin-dependent origin of these dynamics, we remove the microwave π pulse and observe no difference signal [29].

These measurements provide direct observation of spin-dependent PL dynamics in SiC and support previous assumptions that these defects exhibit optical dynamics similar to other OPCCs such as the NV center in diamond. Additionally, we corroborate the variable-length laser-pulse results using time-correlated single-photon counting methods [45,46] and observe a spin-dependent pulsed ODMR contrast of 2.75%. By combining this value with the numerical modeling, we estimate an intrinsic spin-dependent pulsed ODMR contrast of 4.9% for ideal measurement parameters (for details, see Ref. [29]). While this value is lower than typically observed for single NV centers, it is similar to what has been previously observed for high-density NV center ensembles [47] and single defects in other SiC polytypes [1].

IV. CONCLUSIONS AND OUTLOOK

In conclusion, we demonstrate resonant excitation of 3*C*-SiC photonic crystal cavities with integrated defect spins for large PL and ODMR signal enhancements and increased spin initialization rates. Our analysis shows that our present cavity designs are capable of achieving localized optical field intensities that can be enhanced by a factor of almost 200 relative to an incident Gaussian beam. This value could be further improved with concurrent optimization of cavity Q and coupling to the Gaussian excitation mode [48]. For measurements of ensembles of defects, these small mode volumes and excitation intensity enhancements may facilitate on-chip applications that have limited power budgets, inefficient optical coupling, or poor spectral overlap of the excitation source and defect absorption bands. These applications include spin-ensemble-based sensing techniques [40], enhanced absorption for hole-burning experiments

[49], or for enhancing the signal of spectrally distinct subensembles in order to study inhomogeneous broadening [41]. For applications involving single defects, cavity-resonant excitation can provide enhanced optical stark shifts [21], compact, on-chip single-photon frequency conversion [22], or reduced excitation of background impurities that are detrimental to single-photon source performance [33,50,51]. Additionally, we provide evidence that defects in 3*C*-SiC exhibit photodynamics similar to those observed for OPCCs like the NV center in diamond. These results underscore the benefits of fabricating devices with integrated defect spin states in heteroepitaxial 3*C*-SiC as a means to incorporate defect qubits into scalable device architectures for applications in the field of quantum information and sensing.

ACKNOWLEDGMENTS

We thank David Christle, Bob Buckley, and Joerg Bochmann for helpful discussions. This work was supported by the AFOSR QuMPASS MURI FA9550-12-1-004, Office of Naval Research N00014-15-1-2369 and NSF DMR-1306300. A portion of this work was done in the UC Santa Barbara nanofabrication facility, part of the NSF-funded NNIN network. We acknowledge support from the Center for Scientific Computing from the CNSI, MRL: an NSF MRSEC (DMR-1121053) and NSF CNS-0960316.

[1] David J. Christle, Abram L. Falk, Paolo Andrich, Paul V. Klimov, Jawad Ul Hassan, Nguyen T. Son, Erik Janzen, Takeshi Ohshima, and David D. Awschalom, Isolated electron spins in silicon carbide with millisecond coherence times, Nat. Mater. **14**, 160 (2014).

[2] William F. Koehl, Bob B. Buckley, F. Joseph Heremans, Greg Calusine, and David D. Awschalom, Room temperature coherent control of defect spin qubits in silicon carbide, Nature (London) **479**, 84 (2011).

[3] A. Powell, Growth of SiC substrates, Int. J. High Speed Electron. Syst. **16**, 751 (2006).

[4] C. M. Zetterling, *Process Technology for Silicon Carbide Devices*, EMIS Processing Series (INSPEC, Stevenage, 2002).

[5] Marko Lončar and Andrei Faraon, Quantum photonic networks in diamond, MRS Bull. **38**, 144 (2013).

[6] I. J. Luxmoore, N. A. Wasley, A. J. Ramsay, A. C. T. Thijssen, R. Oulton, M. Hugues, S. Kasture, V. G. Achanta, A. M. Fox, and M. S. Skolnick, Interfacing Spins in an InGaAs Quantum Dot to a Semiconductor Waveguide Circuit Using Emitted Photons, Phys. Rev. Lett. **110**, 037402 (2013).

[7] Andrei Faraon, Arka Majumdar, Dirk Englund, Erik Kim, Michal Bajcsy, and Jelena Vučković, Integrated quantum optical networks based on quantum dots and photonic crystals, New J. Phys. **13**, 055025 (2011).

[8] J. E. Kennard, J. P. Hadden, L. Marseglia, I. Aharonovich, S. Castelletto, B. R. Patton, A. Politi, J. C. F. Matthews, A. G. Sinclair, B. C. Gibson, S. Prawer, J. G. Rarity, and J. L. O'Brien, On-Chip Manipulation of Single Photons from a Diamond Defect, Phys. Rev. Lett. **111**, 213603 (2013).

[9] G. Reithmaier, S. Lichtmannecker, T. Reichert, P. Hasch, K. Muller, M. Bichler, R. Gross, and J. J. Finley, On-chip time resolved detection of quantum dot emission using integrated superconducting single photon detectors, Sci. Rep. **3**, 1901 (2013).

[10] Shota Yamada, Bong-Shik Song, Seungwoo Jeon, Jeremy Upham, Yoshinori Tanaka, Takashi Asano, and Susumu Noda, Second-harmonic generation in a silicon carbide–based photonic crystal nanocavity, Opt. Lett. **39**, 1768 (2014).

[11] Marina Radulaski, Thomas M. Babinec, Sonia Buckley, Armand Rundquist, J Provine, Kassem Alassaad, Gabriel Ferro, and Jelena Vučković, Photonic crystal cavities in cubic (3C) polytype silicon carbide films, Opt. Express **21**, 32623 (2013).

[12] Jonathan Y. Lee, Xiyuan Lu, and Qiang Lin, High-*Q* silicon carbide photonic-crystal cavities, Appl. Phys. Lett. **106**, 041106 (2015).

[13] David O. Bracher and Evelyn L. Hu, Fabrication of high-*Q* nanobeam photonic crystals in epitaxially grown 4*H*-SiC, Nano Lett. **15**, 6202 (2015).

[14] Jaime Cardenas, Mian Zhang, Christopher T. Phare, Shreyas Y. Shah, Carl B. Poitras, Biswajeet Guha, and Michal Lipson, High *Q* SiC microresonators, Opt. Express **21**, 16882 (2013).

[15] Andrei Faraon, Charles Santori, Zhihong Huang, Victor M. Acosta, and Raymond G. Beausoleil, Coupling of Nitrogen-Vacancy Centers to Photonic Crystal Cavities in Monocrystalline Diamond, Phys. Rev. Lett. **109**, 033604 (2012).

[16] Luozhou Li, Tim Schrder, Edward H. Chen, Michael Walsh, Igal Bayn, Jordan Goldstein, Ophir Gaathon, Matthew E. Trusheim, Ming Lu, Jacob Mower, Mircea Cotlet, Matthew L. Markham, Daniel J. Twitchen, and Dirk Englund, Coherent spin control of a nanocavity-enhanced qubit in diamond, Nat. Commun. **6**, 6173 (2015).

[17] H. J. Kimble, The quantum internet, Nature (London) **453**, 1023 (2008).

[18] W. Pfaff, B. J. Hensen, H. Bernien, S. B. van Dam, M. S. Blok, T. H. Taminiau, M. J. Tiggelman, R. N. Schouten, M. Markham, D. J. Twitchen, and R. Hanson, Unconditional quantum teleportation between distant solid-state quantum bits, Science **345**, 532 (2014).

[19] Greg Calusine, Alberto Politi, and David D. Awschalom, Silicon carbide photonic crystal cavities with integrated color centers, Appl. Phys. Lett. **105**, 011123 (2014).

[20] Hyun-Joo Chang, Se-Heon Kim, Yong-Hee Lee, Emil P. Kartalov, and Axel Scherer, A photonic-crystal optical antenna for extremely large local-field enhancement, Opt. Express **18**, 24163 (2010).

[21] R. Bose, D. Sridharan, G. S. Solomon, and E. Waks, Large optical stark shifts in semiconductor quantum dots coupled to photonic crystal cavities, Appl. Phys. Lett. **98**, 121109 (2011).

[22] Murray W. McCutcheon, Darrick E. Chang, Yinan Zhang, Mikhail D. Lukin, and Marko Loncar, Broadband frequency conversion and shaping of single photons emitted from a nonlinear cavity, Opt. Express **17**, 22689 (2009).

[23] Ren-Jye Shiue, Xuetao Gan, Yuanda Gao, Luozhou Li, Xinwen Yao, Attila Szep, Dennis Walker, James Hone, and Dirk Englund, Enhanced photodetection in graphene-integrated photonic crystal cavity, Appl. Phys. Lett. **103**, 241109 (2013).

[24] K. Jensen, N. Leefer, A. Jarmola, Y. Dumeige, V. M. Acosta, P. Kehayias, B. Patton, and D. Budker, Cavity-Enhanced Room-Temperature Magnetometry Using Absorption by Nitrogen-Vacancy Centers in Diamond, Phys. Rev. Lett. **112**, 160802 (2014).

[25] X. Liu, T. Shimada, R. Miura, S. Iwamoto, Y. Arakawa, and Y. K. Kato, Localized Guided-Mode and Cavity-Mode Double Resonance in Photonic Crystal Nanocavities, Phys. Rev. Applied **3**, 014006 (2015).

[26] Abram L. Falk, Bob B. Buckley, Greg Calusine, William F. Koehl, Viatcheslav V. Dobrovitski, Alberto Politi, Christian A. Zorman, Philip X.-L. Feng, and David D. Awschalom, Polytype control of spin qubits in silicon carbide, Nat. Commun. **4**, 1819 (2013).

[27] V. Ya. Bratus, R. S. Melnik, S. M. Okulov, V. N. Rodionov, B. D. Shanina, and M. I. Smoliy, A new spin one defect in cubic SiC, Physica (Amsterdam) **404B**, 4739 (2009).

[28] Jun Ye and Theresa W. Lynn, *Applications of Optical Cavities in Modern Atomic, Molecular, and Optical Physics* (Academic Press, Oxford, 2003), pp. 1–83.

[29] See Supplemental Material at http://link.aps.org/supplemental/10.1103/PhysRevApplied.6.014019 for further details of cavity field enhancement calculations and simulations, the experimental setup, control experiments, and additional corroborating measurements.

[30] J. D. Joannopoulos, R. D. Meade, and J. N. Winn, *Photonic Crystals: Molding the Flow of Light* (Princeton University Press, Princeton, New Jersey, 1995).

[31] http://www.Lumerical.com.

[32] Michael Bass, Eric W. Van Stryland, and David R. Williams, *Handbook of Optics* (McGraw-Hill, New York, 1995), Vol. 2.

[33] Masahiro Nomura, Satoshi Iwamoto, Toshihiro Nakaoka, Satomi Ishida, and Yasuhiko Arakawa, Localized excitation of InGaAs quantum dots by utilizing a photonic crystal nanocavity, Appl. Phys. Lett. **88**, 141108 (2006).

[34] F. Jelezko, I. Popa, A. Gruber, C. Tietz, J. Wrachtrup, A. Nizovtsev, and S. Kilin, Single spin states in a defect center resolved by optical spectroscopy, Appl. Phys. Lett. **81**, 2160 (2002).

[35] Jenna Hagemeier, Cristian Bonato, Tuan-Anh Truong, Hyochul Kim, Gareth J. Beirne, Morten Bakker, Martin P. van Exter, Yunqiu Luo, Pierre Petroff, and Dirk Bouwmeester, H1 photonic crystal cavities for hybrid quantum information protocols, Opt. Express **20**, 24714 (2012).

[36] Murray W. McCutcheon, Georg W. Rieger, Iva W. Cheung, Jeff F. Young, Dan Dalacu, Simon Frdrick, Philip J. Poole, Geof C. Aers, and Robin L. Williams, Resonant scattering and second-harmonic spectroscopy of planar photonic crystal microcavities, Appl. Phys. Lett. **87**, 221110 (2005).

[37] W. E. Moerner and T. P. Carter, Statistical Fine Structure of Inhomogeneously Broadened Absorption Lines, Phys. Rev. Lett. **59**, 2705 (1987).

[38] Tian Zhong, Jonathan M. Kindem, Evan Miyazono, and Andrei Faraon, Nanophotonic coherent light-matter interfaces based on rare-earth-doped crystals, Nat. Commun. **6**, 8206 (2015).

[39] Janine Riedrich-Moller, Laura Kipfstuhl, Christian Hepp, Elke Neu, Christoph Pauly, Frank Mucklich, Armin Baur, Michael Wandt, Sandra Wolff, Martin Fischer, Stefan Gsell, Matthias Schreck, and Christoph Becher, One- and two-dimensional photonic crystal microcavities in single crystal diamond, Nat. Nanotechnol. **7**, 69 (2012).

[40] Hannah Clevenson, Matthew E. Trusheim, Carson Teale, Tim Schroder, Danielle Braje, and Dirk Englund, Broadband magnetometry and temperature sensing with a light-trapping diamond waveguide, Nat. Phys. **11**, 393 (2015).

[41] Eric van Oort and Max Glasbeek, Frequency-dependent dephasing of *N-V* centers in diamond, J. Lumin. **53**, 88 (1992).

[42] Marcus W. Doherty, Neil B. Manson, Paul Delaney, Fedor Jelezko, Jrg Wrachtrup, and Lloyd C. L. Hollenberg, The nitrogen-vacancy colour centre in diamond, Phys. Rep. **528**, 1 (2013).

[43] N. B. Manson, J. P. Harrison, and M. J. Sellars, Nitrogen-vacancy center in diamond: Model of the electronic structure and associated dynamics, Phys. Rev. B **74**, 104303 (2006).

[44] Lucio Robledo, Hannes Bernien, Toeno van der Sar, and Ronald Hanson, Spin dynamics in the optical cycle of single nitrogen-vacancy centres in diamond, New J. Phys. **13**, 025013 (2011).

[45] W. Becker, *Advanced Time-Correlated Single Photon Counting Techniques*, Springer Series in Chemical Physics (Springer, Berlin, 2005).

[46] Birgit J. M. Hausmann, Thomas M. Babinec, Jennifer T. Choy, Jonathan S. Hodges, Sungkun Hong, Irfan Bulu, Amir Yacoby, Mikhail D. Lukin, and Marko Lončar, Single-color centers implanted in diamond nanostructures, New J. Phys. **13**, 045004 (2011).

[47] B. J. Maertz, A. P. Wijnheijmer, G. D. Fuchs, M. E. Nowakowski, and D. D. Awschalom, Vector magnetic field microscopy using nitrogen vacancy centers in diamond, Appl. Phys. Lett. **96**, 092504 (2010).

[48] Simone L. Portalupi, Matteo Galli, Christopher Reardon, Thomas Krauss, Liam O'Faolain, Lucio C. Andreani, and Dario Gerace, Planar photonic crystal cavities with far-field optimization for high coupling efficiency and quality factor, Opt. Express **18**, 16064 (2010).

[49] R. T. Harley, M. J. Henderson, and R. M. Macfarlane, Persistent spectral hole burning of colour centres in diamond, J. Phys. C **17**, L233 (1984).

[50] W. E. Moerner and David P. Fromm, Methods of single-molecule fluorescence spectroscopy and microscopy, Rev. Sci. Instrum. **74**, 3597 (2003).

[51] L. C. Bassett, F. J. Heremans, C. G. Yale, B. B. Buckley, and D. D. Awschalom, Electrical Tuning of Single Nitrogen-Vacancy Center Optical Transitions Enhanced by Photoinduced Fields, Phys. Rev. Lett. **107**, 266403 (2011).